A fast data-reduction method for circular-sector electrodiffusion probes for wall-shear-rate measurement

Mouhamad El Hassan, Jaromir Havlica, Walid Blel, Nikolay Bukharin, Vaclav Sobolik

Results in Engineering 32 (2026) 112524

Contents lists available at ScienceDirect

Results in Engineering

journal homepage: www.sciencedirect.com/journal/results-in-engineering

Research paper

A fast data-reduction method for circular-sector electrodiffusion probes for wall-shear-rate measurement

Mouhamad El Hassan [a], Jaromir Havlica [b,c], Walid Blel [d], Nikolay Bukharin [e], Vaclav Sobolik [f,*]

[a] *Prince Mohammad Bin Fahd University, Department of Mechanical Engineering, Al Khobar, Saudi Arabia*
[b] *Institute of Chemical Process Fundamentals, Czech Academy of Sciences, Prague, Czech Republic*
[c] *Faculty of Science, University Jan Evangelista Purkyne, Ústí nad Labem, Czech Republic*
[d] *GEPEA, University of Nantes, CRTT, Saint Nazaire, France*
[e] *The Southern Alberta Institute of Technology (SAIT) Calgary, Alberta, Canada*
[f] *LaSIE UMR - 7356 CNRS, University of La Rochelle, La Rochelle, France*

ARTICLE INFO

Keywords:
Electrodiffusion probe
Circular-sector probe
Wall shear rate
Flow direction
Directional characteristics
Boundary-layer approximation

ABSTRACT

Circular-sector electrodiffusion probes provide multi-electrode current signals for estimating near-wall flow direction and wall shear rate, but their practical use requires a fast, transparent, and uncertainty-aware data-reduction procedure. This study presents a unified calibration-to-inversion framework for two-, three-, and four-sector probes based on pre-calculated universal coefficients and Fourier representations of the directional characteristics. The proposed FastAngle3 / FastAngle4 algorithms use current ranking and local linear interpolation to reconstruct flow direction without iterative optimization, making the method suitable for online processing of time-resolved measurements. The framework is evaluated using archival Couette-flow calibration data for a real three-sector probe at $Pe = 5 \times 10^3$, covering the full 0–360° range in 15° increments. The linearized reconstruction yields a maximum angular deviation below 3.5° The measured total current varies by only 0.221 μA, corresponding to about 1.94% of its mean value. The effects of unequal sector areas, radial diffusion, inter-sector gaps, geometric irregularity, and current noise are examined in terms of their influence on flow-angle and wall-shear-rate estimation. The method therefore advances directional wall-shear-rate measurement by combining compact modelling, non-iterative inversion, calibration-based validation, and uncertainty assessment within a single online-ready workflow. Its applicability is limited to quasi-steady, high-Péclet-number conditions for which the Lévêque boundary-layer approximation remains valid.

1. Introduction

Since the pioneering study of [1], the measurement of wall shear rate $\dot{\gamma}$ by means of the limiting diffusion current is a well-established technique [2–4]. For Newtonian fluids, wall shear rate and wall shear stress carry equivalent information because they differ only by the constant factor of dynamic viscosity. In the following, the notion wall shear rate will be used. The method is based on measuring the limiting diffusion current at a small working electrode flush-mounted in a wall, thereby directly providing the wall shear rate at the wall surface. Multiple electrodes are able to resolve the components of wall shear rate, i.e. identify the flow direction in the wall vicinity. The ability to accomplish this task has previously been shown in the Taylor-Couette-Poiseuille arrangement, using a 3-segmented electrodiffusion probe to obtain measurements of the axial & azimuthal shear rates at the wall boundaries [5]; as well similar multi-component measurements have been made using helical Taylor-Couette flow and with axial through flow [6]. Thus, providing a motivation for developing computationally efficient, on-line possible, methods of data reduction when using directional probes.

Recent electrodiffusion studies across a range of industrially and fundamentally relevant configurations collectively underscore the need for rapid directional data reduction. In Taylor–Couette geometry, Merabet et al. (2025) [7] deployed limiting-current probes to track wall shear rate through successive flow-regime transitions in a two-fluid (immiscible) annular system, a context in which the inferred shear vector changes both magnitude and direction continuously with the

* Corresponding author.
E-mail address: vsobolik@univ-lr.fr (V. Sobolik).

https://doi.org/10.1016/j.rineng.2026.112524
Received 14 August 2026; Accepted 17 August 2026
Available online 18 August 2026

Nomenclature

Symbol	Definition Units
a_{ij}	Fourier cosine coefficient (fitting measured normalized currents)-
$B_0(\alpha)$ z	Zeroth-order Fourier coefficient of $I(\alpha,\ \varphi)$ -
$B_m(\alpha)$	m-th cosine Fourier coefficient of $I(\alpha,\ \varphi)$ -
b_{ij}	Fourier sine coefficient (fitting measured normalized currents) -
c	Concentration of active species $mol{\cdot}m^{-3}$
c_0	Bulk concentration of active species $mol{\cdot}m^{-3}$
C_m	Universal Fourier coefficient of normalized current function-
D	Molecular diffusion coefficient of active species $m^2{\cdot}s^{-1}$
F	Faraday constant $C{\cdot}mol^{-1}$
$G(\beta)$ (β)	Normalized current function for sector angle (β)-
$H(\beta_1, \beta_2)$	Normalized current ratio (sector current / total current) with two parameters (β_1, β_2)-
I_s	Normalized sector current -
$I(\alpha,\ \varphi)$	Normalized sector current as function of half-angle α and orientation φ -
$I_j(\varphi)$	Computed normalized current of sector j -
I_j^+	Measured normalized current of sector j -
$I_{l,k}$	Normalized current at lower bounding point of section k-
$I_{u,k}$	Normalized current at upper bounding point of section k -
$I_p, I_q,\ I_r,\ I_s$	Ordered normalized sector currents within a section -
$i(x)$	Local current density at position $xA{\cdot}m^{-2}$
i_s	Dimensional sector current A
i_A	Dimensional total current A
j	Sector index -
K	Proportionality constant :$i(x) = Kx^{-1/3}A{\cdot}m^{-5/3}$
k	Section index in FastAngle algorithm -
L	Characteristic length of the electrodem
P	Numerical constant defined by $Pe = \dot{\gamma}L^2/D$ -
Pe	Péclet number ($Pe = \dot{\gamma}L^2/D$)-
R	Sector radius m
v_x, v_y, v_z	Velocity components $m{\cdot}s^{-1}$
x	Streamwise coordinate (measured from electrode / sector front edge) m
y	Transverse coordinate along electrode width m
z	Wall-normal coordinatem
α	Half-angle of the circular sector (geometric parameter) rad (or °)
β	Auxiliary angular variable defining sector extent relative to flow Angle measured, Fig. 2 rad
β_1	Starting boundary angle of the sector, $\beta_1 = \varphi - \alpha$, Fig. 2 rad
β_2	Ending boundary angle of the sector, $\beta_2 = \varphi + \alpha$, Fig. 2 rad
$\dot{\gamma}$	Wall shear rates^{-1}
ε	Relative deviation (fractional noise) of sector current at bounding point-
φ	Angle between sector bisector (axis) and flow direction, Fig. 2 rad (or °)

Abbreviations

FastAngle3	Linear angle reconstruction algorithm for three-sector probe
FastAngle4	Linear angle reconstruction algorithm for four-sector probe
DC	Directional characteristics
2 s, 3 s, 4s	Two-sector probe; Three-sector probe; Four-sector probe.

Note: The term sector is used for the portion of a circle bounded by two radii and an arc.

evolving flow state. The bubble-induced modulation of near-wall shear rate has received particular attention: Kashinskii & Vorobyev (2020) [8] and Vorobyev & Kashinsky (2024) [9] mapped the highly non-uniform, azimuthally resolved wall shear rate in a 3 × 3 vertical rod bundle under bubbly flow conditions; Kashinsky & Kurdyumov (2021) [10] characterised the axial and azimuthal shear distribution caused by a stationary gas bubble in an annular channel; Gorelikova et al. (2025) [11] showed that tube inclination angle governs local shear asymmetry in upward gas–liquid flows in a circular tube; and Ezeji & Tihon (2022) [12] resolved near-wall reverse-flow regions induced by large rising bubbles in inclined rectangular channels. In all of these cases the probe signal is inherently direction-dependent and time-varying, placing a premium on fast angular inversion. In the domain of impinging jets, Bode et al. (2020) [13] applied electrodiffusion limiting-current sensors beneath a cruciform nozzle at short stand-off distance to obtain the wall shear rate distribution used for turbulence-model benchmarking — an application where efficient processing of large time-resolved datasets is essential. For turbulent near-wall diagnostics, Wang & Tsuji (2024) [14] exploited a spanwise electrode array to resolve streamwise and spanwise wall shear rate fluctuations and their coupling to near-wall streak dynamics in drag-reducing polymer flows, where statistical reliability depends directly on processing throughput. What each of these applications shares is the need to recover the wall shear vector — magnitude and direction — from multi-electrode current signals on a per-sample basis; the fast, non-iterative inversion framework proposed in the present work is designed to address exactly this computational bottleneck.

The total current of the circular-sector probes is practically independent of the flow direction [15–17], which is a well-known limitation of rectangular multiple electrodes [2,18]. Tihon et al. (2003) [18] used a double-strip (sandwich) electrode consisting of two 0.1 × 1 mm rectangles separated by 0.01 mm to study single air bubbles rising in inclined rectangular channels. Information was obtained on the reverse flow in a liquid film separating the bubble from the wall, capillary waves appearing at the bubble tail, and near-wall flow fluctuations in the bubble wake.

Havlica et al. (2021) [19] revisited the classical Leveque theory for rectangular strip probes by accounting for both axial and transverse components of the wall shear rate. They derived generalised analytical formulas for the effective transfer length and the dimensionless mass transfer coefficient, showing that deviations from the classical solution can be significant for certain parameter ranges. Their work was subsequently extended to two-strip probes by Harrandt et al. (2023) [20], who derived analytical expressions for mass transfer coefficients on both segments and proposed an optimal probe geometry for direction-sensitive measurements. More recently, Harrandt et al. (2024) [21] addressed the twin semicircular probe configuration, establishing a theoretical framework relating measured electric currents to the wall shear rate vector under both frontal and reverse-flow conditions.

The data processing method proposed by Harrandt et al. (2024) [21] was developed for twin-electrode semicircular electrodiffusion probes, whereas this current study focuses on circular multi-sector probes and uses pre-calculated (universal) coefficients to determine flow direction via direct, rapid inversion. These two techniques are complementary. Harrandt et al. [20,21] focused on a specific twin-electrode configuration and its associated workflow, whereas the present method provides a single, compact specification for circular-sector probes with 2–4 segments, designed for online use. The goal of the present work is primarily to develop a computationally inexpensive reconstruction and to generate the directional properties of multi-sector probes from a universal coefficient set, thereby determining the flow angle using simple algebraic relations (or a short lookup/linear solve). Importantly, the proposed simplification does not require runtime ad hoc fitting; the numerical effort is confined to the one-time generation of the coefficients, after which reconstruction is performed purely through analytical/algorithmic steps.

Only two methods of circular-sector probes have been successful to date. Using photolithography, Deslouis et al. (1993) [22] fabricated a two-sector (2 s) electrode with a 300 μm diameter and a 20 μm gap between the semicircular electrodes. The drawback of the photolithographic electrodes, i.e. the necessity to place the current supply on the same side of the support plate, has not been overcome to date. This limits the applicability and calibration of photolithographic probes due to their overall size. Another drawback of these probes is the very thin gold layer (0.15 μm), which makes the cleaning of deposits delicate.

The robust, portable three-sector (3 s) probes consist of three platinum wires with a sector cross-section [17]. They are fabricated as follows. Three platinum wires with a diameter of 0.5 mm are pulled simultaneously through circular wire-drawing dies of gradually diminishing diameter, from 1 mm to 0.5 mm. During the drawing, the wires take a sector shape. Drawing is the most delicate operation, during which wire breakage often occurs. It is necessary to anneal the wires in a gas flame after each drawing pass and to lubricate them with beeswax. The wires are then electrophoretically coated with a polymeric paint to insulate them and are tightly glued together with epoxy resin. After soldering the connecting cables, the wires are glued in a stainless steel tube with a tip diameter of 5 mm or smaller. The tip is then ground with emery paper and polished. The surface of these probes can be cleaned practically without limitation. The geometrical perfection of the probes has been improved over time. Compare the probes used in early experiments [23], with the probe discussed in this paper and the nearly perfect probe [24]. Only 3 s probes can be fabricated using the wire-drawing method. The experiments involving two wires resulted in an unstable positioning of the wires in the die, leading to twisting. The behaviour of the four wires in the dies is similar. Moreover, there is no need to use small four-sector (4 s) probes instead of 3 s ones in wall shear rate measurements. The three sector currents are sufficient to resolve two components of wall shear rate and the normal velocity component [25–27].

Wein & Wichterle (1989) [28] analysed the current distribution in three-sector probes with insulating insertions theoretically and presented it in a form suitable for numerical computation. Using a finite-difference method with an oblate-spheroidal coordinate system, Geshev & Safarova (1999) [29] calculated the steady-state, transient, and angular characteristics of circular-sector probes. They accounted for diffusion in both longitudinal and transverse directions. Lamarche-Gagnon et al. (2018) [24] used mass-transfer data from a three-sector electrodiffusion probe to infer the instantaneous components of the wall shear rate via an inverse problem. They numerically evaluated the impact of gap size on the DC of the 3 s probe.

Harrandt et al. (2024) [21] have developed a new framework for working with directionally sensitive, twin semicircular probes in both frontal and reverse flows. This work aims to provide a solution to an alternative requirement—reconstructing the two-dimensional (2D) flow field using multi-sector circular probes (2–4 sectors)—by offering a low-complexity reconstruction method using universal coefficients and a compact Fourier representation of the directional response. As such, these two methods will differ in geometry and emphasis; the Harrandt et al. [20,21] study prioritizes higher accuracy for a specific geometry (two-electrode design), while our study emphasizes reduced time to collect and use data across multiple geometries (multi-sector probe).

The goal of this paper is to develop a clear method for predicting sector currents in quasi-steady boundary-layer flows, with particular emphasis on online reduction of wall-shear measurement data. The novelty does not lie in introducing a new electrodiffusion measurement principle, but in reorganizing the established theory into a unified and computationally inexpensive calibration-to-inversion workflow for circular probes with two, three, or four sectors. Unlike iterative inverse approaches, the proposed method identifies the angular interval from the ordering of the measured currents and reconstructs the flow angle through direct interpolation using precomputed calibration bounds. Three original contributions are presented: (1) a compact, unified formulation based on universal (pre-calculated) coefficients that describes the directional characteristics of 2–4-sector circular electrodiffusion probes; (2) a non-iterative procedure for obtaining the flow angle from algebraic relations, including a linearized form of the directional characteristics for fast estimation; and (3) a practical analysis of key non-idealities—radial diffusion, inter-sector gaps, and geometric irregularities—quantifying their influence on the total current and the resulting wall-shear-rate estimate. The term sector denotes the portion of a circle bounded by two radii and an arc (rather than a segment). The approach is validated using calibration data from a three-sector probe, which also provides guidance for identifying the relevant flow-direction interval and implementing the reconstruction in real time. Therefore, the proposed method was assessed not only analytically but also through real-world experimentation and practical robustness testing.

2. Theoretical analysis

2.1. Electrodiffusion method

The measuring system consists of a small working electrode, a large auxiliary electrode, a solution containing a depolarizer and an excess of supporting electrolyte, and a multi-channel potentiostat controlled by a computer. The reference electrode used in analytical electrochemistry for precise potential control between the working and auxiliary electrodes is omitted. The potential is determined experimentally from the plateau on the current-voltage scan. The presence of the plateau confirms that only the active species react on the working electrode. In this case, the electric current is limited by the diffusion of active species to and from the working electrode. The equation of steady diffusion

$$\boldsymbol{v}\cdot\nabla c = D\nabla^2 c, \tag{1}$$

can be simplified under the assumption $v_x = \dot{\gamma}\,z,\ v_y = v_z = 0$ to

$$\dot{\gamma}z\,(\partial c/\partial x) = D\,\left(\partial^2 c/\partial x^2 + \partial^2 c/\partial y^2 + \partial^2 c/\partial z^2\right) \tag{2}$$

If the Peclet number ($Pe = \dot{\gamma}\cdot L^2/D$, L is the characteristic length of the electrode) is high, the terms of longitudinal $\left(\partial^2 c/\partial_{xx}\right)$ and transversal $\left(\partial^2 c/\partial_{yy}\right)$ diffusion can be omitted. The resulting boundary layer problem with the boundary conditions

$$c = c_0 \text{ for } z = \infty \text{ or } x = 0;\ c = 0 \text{ for } x > 0 \text{ and } z = 0,$$

has an analytic solution using similarity transformation [30]

$$c(x,y,z) = c_0\ C_w(w) \text{ and } w = z(9\ Dx/\dot{\gamma})^{-1/3} \tag{3}$$

The local current density calculated from the resulting concentration gradient, $i(x) = nFD\ (dc/dz)_{x,\ z=0}$ (n is the number of electrons involved in the reaction and F stands for the Faraday constant), is expressed by the relation

$$i(x) = K\ x^{-1/3} \tag{4}$$

$$K = nFc_0 D^{2/3}(\dot{\gamma}/9)^{1/3}\Big/\Gamma(4/3)\ = 0.5383660549\ nFc_0\ D^{2/3}\ \dot{\gamma}^{1/3} \tag{5}$$

It should be emphasized that x is measured from the electrode's front edge. According to Eq. (4), the current density at $x = 0$ is infinite. The finite rate of the electrochemical reaction and the electric resistance of the electrolyte make this current finite. The principle of flow direction resolution for sector electrodes is based on the fact that the current density decreases with x-1/3 (Fig. 1).

It holds for the current through the first segment 1 with a width dy

$$di_1 = (3\,/\,2)\;K\;\left(x_1^{2/3}\right)\;dy\;=\;0.807549\;nFc_0\;D^{2/3}\;\dot{\gamma}^{1/3}\;\left(x_1^{2/3}\right)\;dy \tag{6}$$

The current di_2 through the second segment,

$$di_2 = (3\,/\,2)\;K\;\left(x_2^{2/3} - x_1^{2/3}\right)\;dy \tag{7}$$

is equal to the sum of currents through both segments (total electrode) minus the current through the first segment.

The formulation presented in this section is for quasi-steady wall-bounded flows under the boundary-layer assumption and depicts the electrodiffusion process at a high Péclet number. It has also been assumed that convection and wall-normal diffusion dominate mass transfer within the thin diffusion layer and that longitudinal and transverse diffusion terms are negligible in the first approximation. The proposed directional-characteristic model and the associated fast inversion procedure will work well when the direction of wall shear rate changes very slowly relative to the time required for the diffusion layer to respond, and when the diffusion layer is thin compared to the probe radius. Caution should be taken when using the method when these assumptions are not satisfied, such as in low Péclet number conditions, or in flows that are strongly unsteady, rapidly reversing, or in configurations that have significant geometric non-idealities (e.g. wide gaps between sectors), for which additional correction terms or a full convection-diffusion analysis may be required.

2.2. Flow situation

The flow situation is presented in Fig. 1. The flow has only one velocity component, v_x, which is parallel to the wall and electrode surface. The velocity profile in the concentration boundary layer has a constant gradient, the wall shear rate $\dot{\gamma}$. The electrode, composed of two insulated segments 1_1, 1_2, is flush-mounted to the surfaces 2 and 3, which can serve as auxiliary electrodes.

2.3. Sector current

The geometry of a sector with the radius R is defined by the half angle α (Fig. 2). The sector makes the angle φ with the uniform steady flow field v_x. We shall introduce alternative pairs of parameters

$$\beta_1 = \varphi - \alpha \text{ and } \beta_2 = \varphi + \alpha, \tag{8}$$

for the computation of the electrical current i_s through the segment. The conditions $\alpha < \pi$ and $\beta_2 > \beta_1$ are expressed by the constraint $0 < \beta_2 - \beta_1 < 2\pi$.

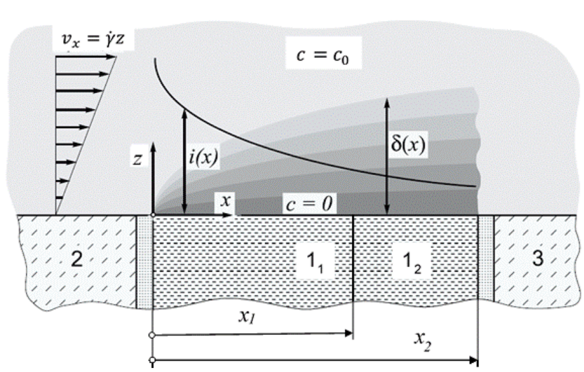

Fig. 1. Section view of the wall 2, 3 with electrode segments 1_1, 1_2, velocity field v_x, concentration boundary layer $\delta(x)$ and current density $i(x)$.

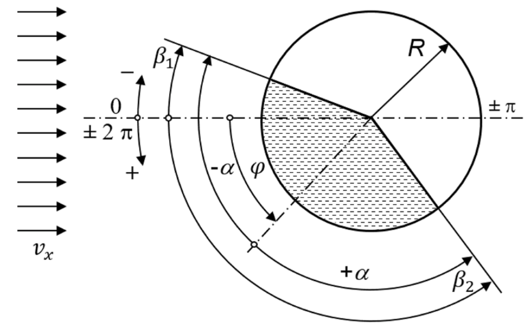

Fig. 2. Geometry of a sector in the flow field.

The ratio of the currents through a segment to the total current is the normalized current $I_s = i_s/i_A$, which depends only on the angles $\beta_1$and β_2 or φ and α

$$I_s = H(\beta_1,\;\beta_2) = H(\varphi - \alpha,\;\varphi + \alpha)\;. \tag{9}$$

There are eight distinct types of sector, differing in both size and orientation (Fig. 3).

The computation of H values for different sectors is based on the following rules:

$$H(\beta,\;\beta + 2\pi) = 1, \tag{10}$$

$$H(\beta_1,\;\beta) + H(\beta,\;\beta_2) = H(\beta_1,\;\beta_2), \tag{11}$$

$$H(2\pi - \beta_2,\;2\pi - \beta_1) = H(\beta_1, \beta_2). \tag{12}$$

The H value of segment with an angle of 2π equals to the whole electrode (Eq.10). The sum of H of two adjacent segments is equal to the whole segment (Eq.11). The H values of the segments that are mirror-symmetric with respect to the x-axis are equal (Eq.12).

Using these rules, the H value of two arguments can be expressed by a function G with a single argument

$$G(\beta) = H(0, \beta),\;0 < \beta < \pi. \tag{13}$$

The calculation of normalized currents, $H(\beta_1, \beta_2)$, for eight types of sectors (Fig. 3) is summarized in Table 1.

There are two cases for the function $\beta < \pi/2$ and $\beta > \pi/2$ (Fig. 4).

There are two expressions for the length of streamlines x_1 crossing a sector in dependence on y.

$$x_1(y) = \left(R^2 - y^2\right)^{1/2} - y\;\mathrm{cotg}\;\beta,\;0 < y < y_s, \tag{14}$$

$$x_1(y) = 2\left(R^2 - y^2\right)^{1/2},\;y_s < y < R, \tag{15}$$

where

$$y_s = R\;\sin\beta. \tag{16}$$

As the concentration boundary layer starts at the front line $(0,\;\pi/4)$ of the sectors (Fig. 4), the length of streamlines Eqs (14) and 15 is the length of the active area. The current through the sectors, i_S, can be calculated using these lengths and Eq.6.

$$i_S = \frac{3}{2}K\int_0^{y_s}\left[\left(R^2 - y^2\right)^{1/2} - y\mathrm{cotg}\beta\right]^{2/3} dy,\;\beta \le \pi\Big/2, \tag{17}$$

$$i_S = \frac{3}{2}KR^{5/3}S\int_0^1\left[\left(1 - (St)^2\right)^{1/2} - Ct\right]^{2/3} dt\;.$$

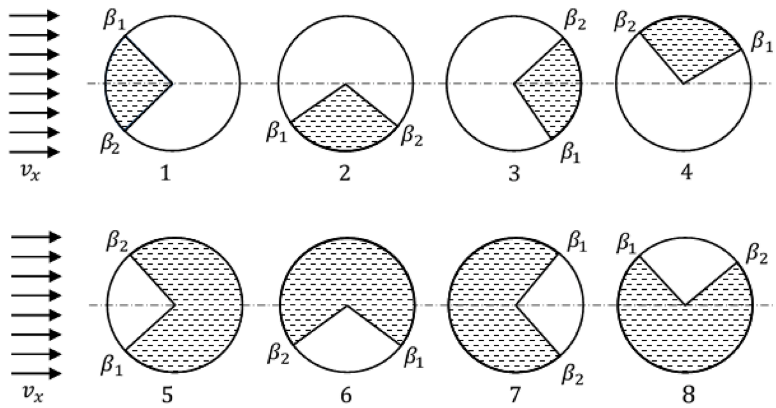

Fig. 3. Eight types of electrode sectors.

Table 1
Representation of $H(\beta_1,\beta_2)$ in terms of function $G(\beta)$ on eight domains.

Case	Conditions	Representation of $\boldsymbol{H}(\beta_1,\beta_2)$
1	$-\pi/2<\beta_1<0<\beta_2<\pi/2$	$G(\beta_2)+G(-\beta_1)$
2	$0<\beta_1<\beta_2<\pi$	$G(\beta_2)-G(\beta_1)$
3	$0<\beta_1<\pi<\beta_2<2\pi$	$1-G(2\pi-\beta_2)-G(\beta_1)$
4	$\pi<\beta_1<\beta_2<2\pi$	$-G(2\pi-\beta_2)+G(2\pi-\beta_1)$
5	$-2\pi<\beta_1<-\pi<\beta_2<0$	$1-G(-\beta_2)-G(2\pi+\beta_1)$
6	$-2\pi<\beta_1<-\pi,\ 0<\beta_2<\pi$	$1+G(\beta_2)-G(2\pi+\beta_1)$
7	$-\pi<\beta_1<-\pi/2,\ \pi/2<\beta_2<\pi$	$G(\beta_2)+G(-\beta_1)$
8	$-\pi<\beta_1<0,\ \pi<\beta_2<2\pi$	$1-G(2\pi-\beta_2)+G(-\beta_1)$

$$i_S=\frac{3}{2}K\left\{\int_0^{y_s}\left[\left(R^2-y^2\right)^{1/2}-y\operatorname{cotg}\beta\right]^{2/3}dy+\int_{y_s}^{R}\left[2\left(R^2-y^2\right)^{1/2}\right]^{2/3}dy\right\},\ \beta\geq\pi\Big/2. \tag{18}$$

$$i_S=\frac{3}{2}KR^{5/3}S\int_0^1\left[\left(1-(St)^2\right)^{1/2}-Ct\right]^{2/3}dt+\frac{3}{2}K\,2^{2/3}R^{5/3}\int_S^1\left(1-t^2\right)^{1/3}dt.$$

where the substitutions $y=y_s\,t$ and $y=R\,t$ were used and $S=\sin\beta$ and $C=\cos\beta$.

Using Eq.18, the total current through a circular electrode is calculated as the sum of the currents of two demi-circles ($\beta=\pi$)

$$i_A=\frac{3}{2}K\,R^{5/3}2^{5/3}\int_0^1\left(1-t^2\right)^{1/3}dt=\frac{3}{2}K\,R^{5/3}P, \tag{19}$$

where, $P=2^{5/3}\int_0^1\left(1-t^2\right)^{1/3}dt=2.670{,}990$. This corresponds to the well-known result [2]

$$i_A=\ 2.15695\ n\ Fc_0D^{2/3}\dot{\gamma}^{1/3}\ R^{5/3}. \tag{20}$$

The function $G(\beta)=i_S/i_A$ is then expressed as

$$G(\beta)=S\Big/P\int_0^1(u-Ct)^{2/3}dt,\ \beta\leq\pi\Big/2 \tag{21}$$

$$G(\beta)=S\Big/P\int_0^1(u-Ct)^{2/3}dt\ +2^{2/3}\Big/\ P\int_S^1\left(1-t^2\right)^{1/3}dt,\ \beta\geq\pi\Big/2\quad, \tag{22}$$

where $u=(1-S^2\,t^2)^{1/2}$.

2.4. Normalized current of sector

It holds for the normalized current $I_S=i_S/i_A$ through a sector characterized by the half angle α and orientation φ

$$I_S(\alpha,\ \varphi)=H(\varphi-\alpha,\ \varphi+\alpha) \tag{23}$$

Functions $G(\beta)$ were calculated using numerical integration (function inttrap in Scilab). The normalized current was expressed from $G(\beta)$ using Table 1. The resulting function $I_S(\alpha,\ \varphi)$ divided by $\sin\alpha$ is shown in Fig. 5 for four values ($\pi/6,\ \pi/4,\ \pi/3$ *and* $\pi/2$) of half angle α, i.e. for the first segment of six, four, three and two-sector electrode. The x-coordinate is $\cos\varphi$. As $I_S(\alpha,\ \varphi)/\sin\alpha$ are almost straight lines, we can suppose that $I_S(\alpha,\ \varphi)$ can be represented by a Fourier series containing only $\cos m\varphi$ terms. These lines are practically parallel which indicates the dependences of coefficients only on $\sin\alpha$. These assumptions were confirmed by the fact that $\int_0^{\pi}I_S(\alpha,\ \varphi)\ d\varphi\ =\alpha$ for each α.

The function $I_S(\alpha,\ \varphi)$ was then expressed by Fourier series

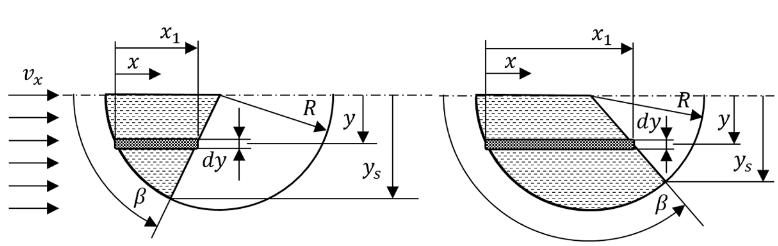

Fig. 4. Two types of sectors for the calculation of the normalized current (function G): a) $\beta\langle\pi/2$. b) $\beta\rangle\pi/2$.

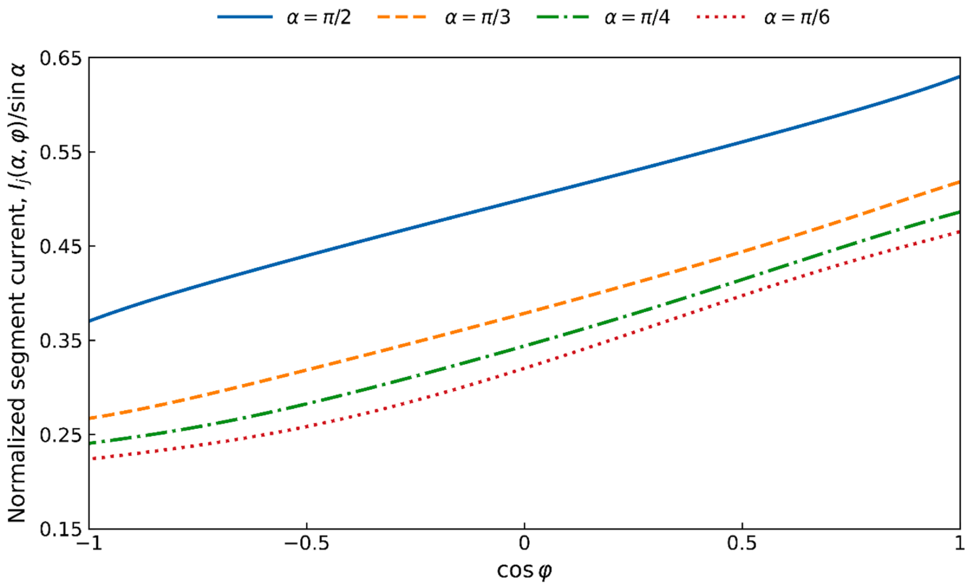

Fig. 5. Normalized segment currents $I_j(\alpha, \varphi)/\sin\alpha$ as function of $\cos\varphi$ for sector half-angles $\alpha = \pi/2, \pi/3, \pi/4,$ and $\pi/6$.

$$I(\alpha,\varphi) = B_0(\alpha) + \sum_{m=1}^{\infty} B_m(\alpha)\cos(m\varphi) \tag{24}$$

where

$$B_0(\alpha) = 1 \Big/ \pi \int_0^{\pi} I(\alpha,\varphi)d\varphi \; = \alpha \Big/ \pi \tag{25}$$

$$B_m(\alpha) = 2 \Big/ \pi \int_0^{\pi} I(\alpha,\varphi)\cos(m\varphi)d\varphi \; = C_m \sin(m\alpha) \tag{26}$$

The universal coefficients C_m are shown in Table 2.

The normalized currents for the first sector in Fig. 5, were calculated for $\varphi \in (0,\ \pi)$, as the function $\cos\varphi$ is even, the mirror symmetry can be used for $\varphi \in (\pi,\ 2\ \pi)$

$$I(\pi < \varphi < 2\pi) = I(2\pi - \varphi). \tag{27}$$

2.5. Directional characteristics of ideal sector probes

The ideal 4 s probe is shown in Fig. 7. The axis of the first sector makes an angle φ_0 with the direction of flow at the beginning. It is an optional setting of the electrode as a whole. The segment currents are computed as a function of the angle φ. The axis of each sector in a multisector probe is shifted by the half-angle of the preceding sector and the half-angle of the current sector. An ideal probe has all sectors identical. By definition, the sum of the normalized sector currents, whether computed $I_j(\varphi)$ or measured $I_j^+(\varphi)$, is unity.

The directional characteristics of the multisegment probe present functions $I_j(\varphi)$ expressing current-direction dependences of the segments. Generally, the determination of the flow angle φ from measured currents I_j^+ presents a solution of the non-linear system

Table 2
Universal coefficients C_m.

M	C_m	m	C_m
1	0.1261380668	5	0.0005038701
2	0.0070158783	6	0.0001517869
3	−0.0030289053	7	−0.0001511711
4	−0.0006405002	8	−0.0000539293

$$I_j(\varphi) - I_j^+ = 0. \tag{28}$$

Use of some properties of the directional characteristics simplifies largely this task. The directional characteristics of the ideal four-segment probe are shown in Fig. 8 for the case $\varphi_0 = 0$. There are four currents $I_j,\ j = 1,\ 2,\ 3,\ 4$ shifted by an angle of $90^\circ(2\alpha)$. The domain 360° is divided into 8 sections, $= 1,\ 2\ ..\ 8$, bounded by the current intersections at $(I_{l,r},\ \varphi_{l,k})$ and $(I_{u,r},\ \varphi_{uk})$. In each section, the condition

$$I_p < I_q < I_r < I_s, \tag{29}$$

is fulfilled for only one permutation of indexes. For example, it holds in the first section, $k = 1, I_3 < I_2 < I_4 < I_1$ and $I_r = I_4$. Comparing the four measured currents, the section k containing the unknown angle is identified. In the next step, we approximate the lines connecting the bounds of the current $I_r = 0.243$ and 0.315 by straight line. We shall call these lines linear DC. The angle φ is close to the solution of the linear equation

$$I_r^+ = I_{l,k} + (I_{u,k} - I_{l,k})\ (\varphi - \varphi_{l,k})\ /\ (\varphi_{u,k} - \varphi_{l,k}), \tag{30}$$

with an accuracy better than 1.3°

The FastAngle procedure is summarized in Fig. 6. The measured sector currents are first compared to identify the angular section k. The corresponding interpolation current I is then selected, and the flow angle is calculated by linear interpolation between the stored section bounds using Eq. (30). The detailed FastAngle3 and FastAngle4 implementations are provided in Appendices A1 and A2.

Here, “online” means that, once the calibration bounds have been determined and stored, each new set of sector currents is converted into a flow angle using only current comparisons and one linear interpolation, without iterative optimization or repeated numerical integration.

A similar procedure for angle estimation can be applied to a 3 s probe. There are only three currents $(I_p < I_q < I_r)$ and six sections k, see Fig. 9. The application of Eq. (30) for the middle current I_q^+ gives the flow angle φ with an accuracy better than 1.5° The slope $\Delta I/\Delta\varphi$ in Eq.30 of the three-sector probe (0.104 rad^{-1}) is greater than the corresponding value for the four-sector probe (0.091 rad^{-1}). This means that the angular resolution of the measured current is better when using the three-sector probe. The larger sections (60°) of the three-sector probes can be advantageous compared to 45° of the four-sector probes.

For the sake of completeness, there are directional characteristics of

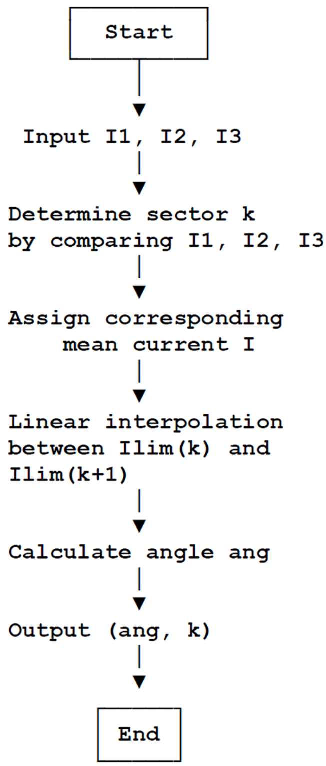

Fig. 6. FastAngle workflow for non-iterative flow-angle reconstruction from measured sector currents.

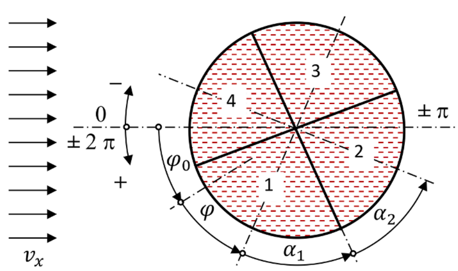

Fig. 7. Ideal four-sector probe.

two-sector probe in Fig. 10. The characteristics can be divided into four sections. As the current permutations in two (1, 4) and two (2, 3) sections are the same, it is impossible to distinguish the flow angle in the whole 360° range. The linear solution for flow angle, Eq. (30), can be applied only on a limited range of angles in the vicinity of the current intersections. The two-sector probes can be used in non-reversing flows.

3. Directional characteristics of real sector probes and experimental validation

Real-sector probes exhibit geometric imperfections such as non-circularity, finite and irregular inter-sector gaps, and unequal sector areas, see Fig. 11. Therefore, each real probe should be calibrated under steady laminar-flow conditions over the angular range in which it will be used. The directional calibration consists of measuring the individual sector currents at a constant wall shear rate while rotating the probe over 0–360°.

The validation data used in the present study are archival measurements reported by Sobolík [17], rather than new measurements. They were obtained in laminar Couette flow between a rotating inner cylinder of diameter 57.6 mm and a stationary outer cylinder of diameter 60.7 ± 0.2 mm. A three-sector probe of 0.5 mm diameter was flush-mounted in the outer-cylinder wall and rotated in 15° increments relative to the steady azimuthal flow. The inner cylinder rotated at 6.7 rpm, corresponding to a wall shear rate of approximately 15 s^{-1}. The electrolyte was an aqueous equimolar potassium hexacyanoferrate (III)/(IV) solution with 1.5% by weight K_2SO_4 as supporting electrolyte and 3% by weight Emkarox 45. At 23 °C, its dynamic viscosity was 2.52 mPa·s, density was 1024 kg·m^{-3}, and ionic diffusivity was 7.5×10^{-10} m^2·s^{-1}, giving $Pe = 5 \times 10^3$. The measured currents are listed in Appendix A3.

Fig. 12 provides an overview of the calibration-to-model workflow, which comprises triplet measurements, Fourier smoothing for reconstruction, and multiple adjustments to create a real probe, including differences in sector sizes, radial diffusion, and inter-sector gaps.

The application of linearized DC for angle resolution is described in the following paragraphs. The measured normalized currents were fitted using a fourth-order Fourier series

$$I_j = a_{0j} + a_{1j}\cos\varphi_j + b_{1j}\sin\varphi_j + a_{2j}\cos 2\varphi_j + b_{2j}\sin 2\varphi_j \cdots + a_{4j}\cos 4\varphi_j + b_{4j}\sin 4\varphi_j \quad (31)$$

The fourth-order expansion was selected after comparing Fourier fits of increasing order. Higher-order terms reduced the fitting residual only marginally, while making the calculated current-intersection points more sensitive to local variations in the calibration data. The fourth-order representation therefore provides a suitable compromise between fitting accuracy, smoothness, and stable identification of the section bounds required by the FastAngle algorithm.

The resulting coefficients a_{ij} and b_{ij} are given Table 3.

The measured normalized currents and their fourth-order Fourier fits are shown together in Fig. 12 (symbols and full lines, respectively), providing the smoothed directional characteristics used as input for section-bound identification (Table 4) and subsequent angle reconstruction.

The unequal sector area has an effect on the measured half angles assigned to each sector, and the theoretical directional characteristics (shown as dashed lines in Fig. 12) are based on universal coefficients so that direct comparisons can be made with the experimental DC.

The next step was the identification of the section bounds I_{lk}, φ_{lk} and I_{uk}, φ_{uk}. These bounds obtained as crossing points of Fourier series Eq. (31) are presented in Table 4 in the form of input data for the algorithm FastAngle3 in Annex. The algorithms were derived for the segment's permutation and sense of probe rotation specified in Figs. 2 and 7. The algorithm must be adapted to the actual probe configuration.

The measured DC were approximated using the universal coefficients C_m, Table 2. The slightly different sector areas were reflected by the unequal half-angles: $\alpha_1 = 61.5°$, $\alpha_2 = 60°$, $\alpha_3 = 58.5°$ The shift angle φ_0 was 186° relative to the ideal probe Fig. 9. The differences between measured and calculated DC are rather large. Using the results of Geshev and Safarova (1999) [29], the DC were corrected for radial diffusion. The relative attenuation of amplitudes was estimated according to Fig. 8 in [29] for $Pe = 5.10^3$ having their corrected DC shown in Fig. 12 (dash-dot), which illustrates an improvement over the universal coefficient (non-corrected) in relation to its accuracy. The correction was applied relative to the pivot value 1/3. The values above and below 1/3 were multiplied by 0.83 and 0.85, respectively.

The amplitudes of the measured currents remained still lower than the amplitudes of the currents corrected for radial diffusion. These differences are attributed to the finite gaps between the segments. The slight local maximum of I_j^+ in the lower part of DC observed at φ = 120° and 240° can be explained by "fresh" solution entering the sector from the inert gap.

After radial-diffusion adjustments, all remaining differences in amplitude were due to gaps between sectors. In addition, Fig. 12 contains pictorial evidence of the systematic drop in amplitude as well as the localized distortions (such as the slight bump in I_1^+) — see experimental DC and corrected theoretical curves for comparison.

Hence, the primary validation figure for the actual probe is Fig. 12:

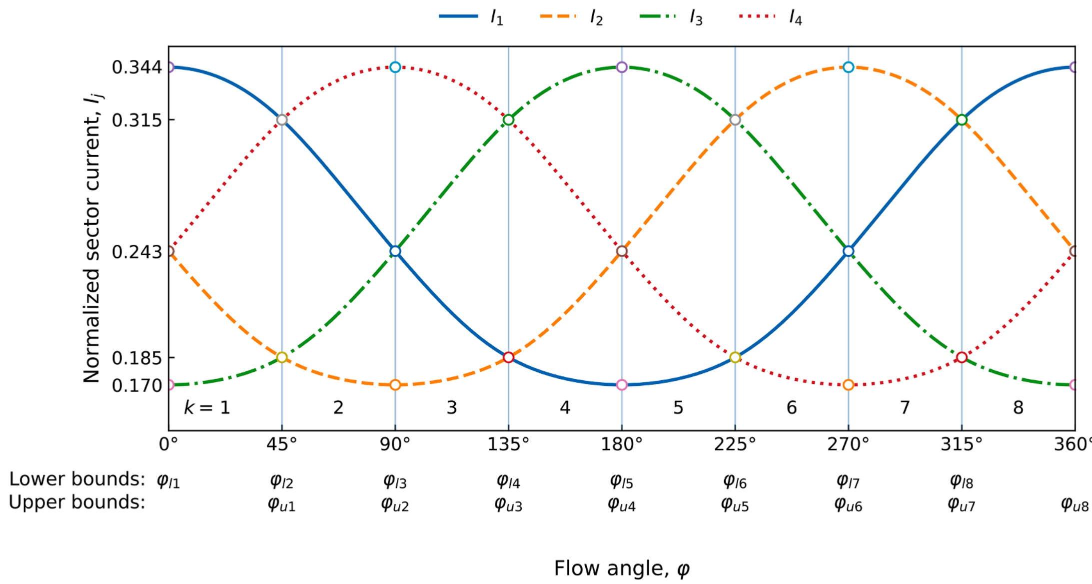

Fig. 8. Directional characteristics of ideal four-sector probe. The 0 – 360° range is divided into eight sections, k = 1, …, 8, bounded by successive current-intersection points denoted by the lower and upper angular limits φ_{lk} and φ_{uk} respectively.

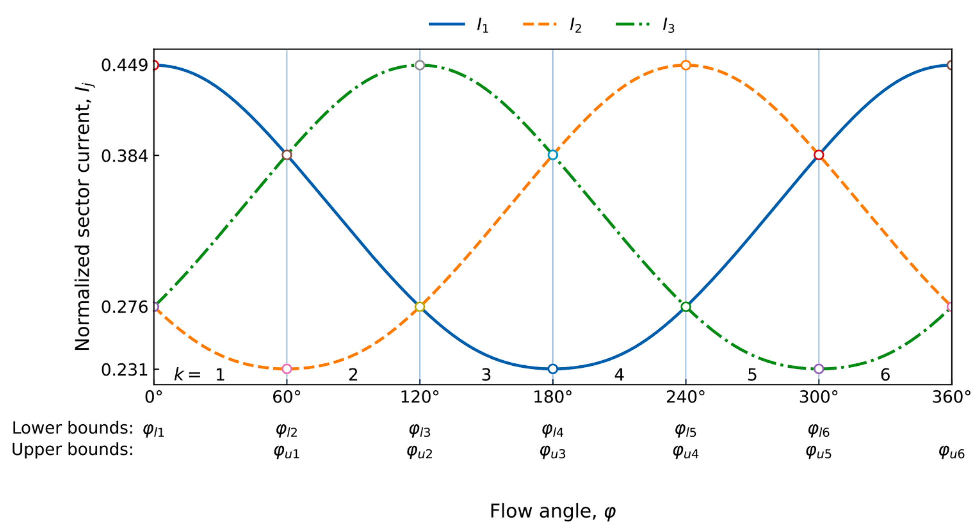

Fig. 9. Directional characteristics of ideal three-sector probe. The 0 – 360° range is divided into six sections, k = 1, …, 6, bounded by successive current-intersection points denoted by the lower and upper angular limits φ_{lk} and φ_{uk} respectively.

calibration data, Fourier representation used for reconstruction, and physical effects (unequal sector area, radial diffusion, gaps) necessary to accurately measure and interpret directionality.

The total current (i_1+i_2+i_3) measured during Couette-flow calibration as a function of probe angle (φ) (See Appendix A3) is shown in Fig. 13. The data points in symbols represent experimental data, while the total current (solid line) is generated from a fourth-order Fourier fit to the data points. The peak-to-peak difference between the two points generated by the total current (0.221 μA, ≈ 1.94% of the mean) shows weak dependence of the total current on the flow direction, while indicating that some geometric imperfections (the probe's geometric irregularity and/or inter-sector gapping) were present.

Using the archival calibration data [17] for the probe shown in Fig. 11, the angular deviation produced by the linearized directional-characteristic method was evaluated over the full 0–360° range. As shown in Fig. 14, the deviation is zero at the section bounds and reaches its largest magnitude between adjacent bounds. For the real three-sector probe, the maximum absolute deviation remains below 3.5° By comparison, the corresponding ideal three-sector probe gives a maximum deviation below 1.5°

The inverse slope $(\varphi_{ui} - \varphi_{li})/(I_{ui} - I_{li})$ of lines connecting the bounding points indicates the robustness of the presented linear method to electrical noise. This slope makes for four- and three-sector ideal probes 627 and 552 deg/-, respectively. This means that three-sector probes are less sensitive to current noise in their angle measurement than four-sector probes.

We shall now estimate the sensitivity of the linear method to sector current noise. Considering ε increase of the current i_1, while i_2 and $i_3$remain constant, the normalized current becomes

$$I_1' = (i_1 + \varepsilon i_1)/(i_1 + i_2 + i_3 + \varepsilon i_1) = (1 + \varepsilon)\ I_1/(1 + \varepsilon I_1).$$

This expression shows that the variation of I_1depends on its initial value and cannot be uniquely determined without additional assumption on the current distribution among the probe segments. For small variations, a first-order approximation gives

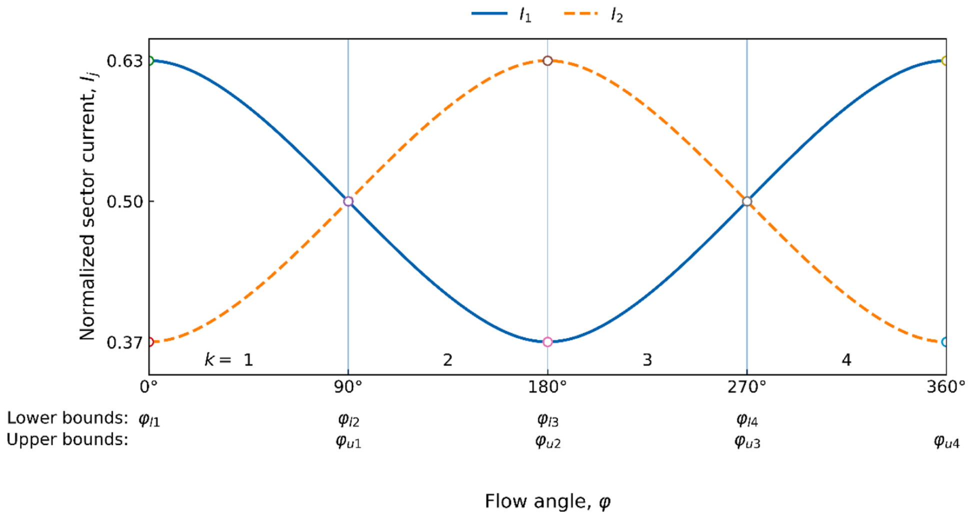

Fig. 10. Directional characteristics of ideal two-sector probe. The 0 – 360° range is divided into four sections, k = 1, …, 4, bounded by successive current-intersection points denoted by the lower and upper angular limits φ_{lk} and φ_{uk} respectively.

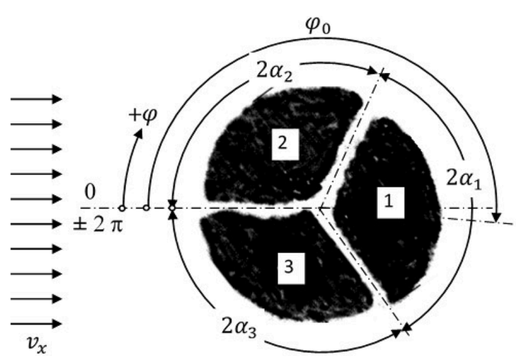

Fig. 11. Three-sector probe of 0.5 mm diameter used in the archival Couette-flow calibration of Sobolík [17]. The rotation of the probe during calibration is in the sense $+\varphi$.

$\Delta I_1 = \varepsilon\, I_1 (1 - I_1).$

Multiplication of the normalized-current variation by the inverse slope of the line connecting adjacent section bounds gives the corresponding angular deviation. Table 5 reports illustrative results for imposed sector-current deviations of 3% and 6% at the bounding points of ideal three- and four-sector probes. These values are used as sensitivity levels and should not be interpreted as a complete experimental uncertainty budget. The three-sector probe shows slightly lower angular sensitivity to current perturbations than the four-sector probe.

Real-sector probes exhibit geometrical imperfections, such as non-circularity, unequal sector area, and insulation gaps. The effect of geometric imperfections (e.g., gaps/irregularities) on measurement as a function of flow-angle extent is illustrated in Fig. 15, showing the wall-shear-rate deviation versus angle; the angular range(s) of maximum effect can be determined for the actual probe geometry from the plot.

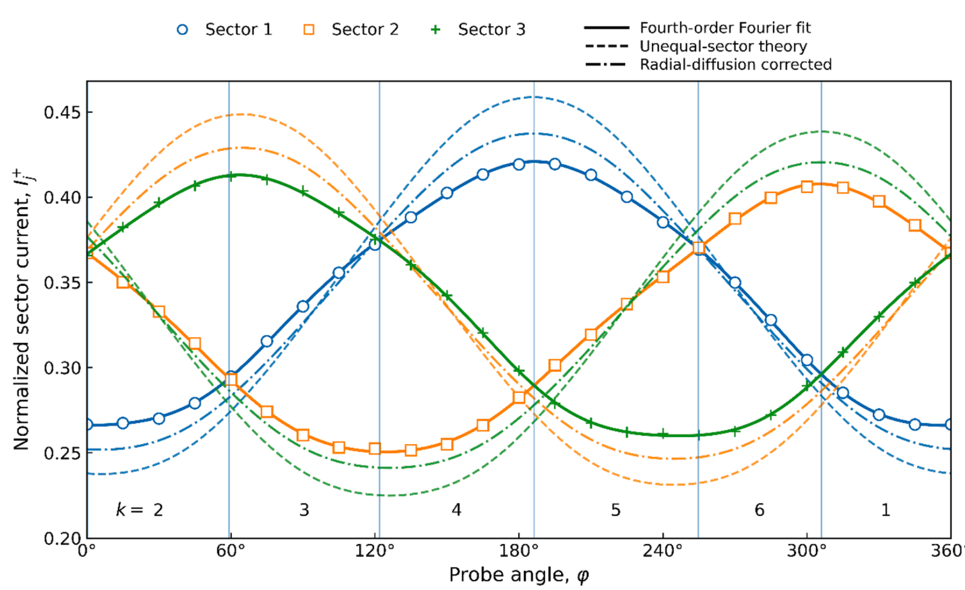

Fig. 12. Directional characteristics obtained from the archival Couette-flow calibration data of Sobolík [17] for the three-sector probe shown in Fig. 11. Normalized currents I_j^+: ○ - first sector, □ - second sector, + - third sector. Dashed lines – theoretical currents taking into account different area (angle) of sectors. Dash-dotted lines - the later currents corrected on radial diffusion [29]. Full lines – Fourier series of fourth order approximated normalized currents. k – sections for angle calculation.

Table 3
Coefficients of Fourier series fitting measured normalized currents.

j	a_{0j}	a_{1j}	b_{1j}	a_{2j}	b_{2j}	a_{3j}	b_{3j}	a_{4j}	b_{4j}
1	0.340649	−0.07797	−0.00664	8.22E-06	0.001677	0.000916	0.00023	0.002462	0.000783
2	0.325638	0.044356	−0.06286	0.000435	−0.00164	−0.00161	−0.00035	−0.0014	0.001602
3	0.333712	0.03361	0.069496	−0.00044	−3.6E-05	0.000698	0.00012	−0.00106	−0.00239

Table 4
The section bounds I_{lk}, φ_{lk} and I_{uk}, φ_{uk} of directional characteristics, Fig. 12.

k		1	2	3	4	5	6
angle°	−54.02	0.4245	59.256	121.84	186.3	254.66	305.98
current	0.2961	0.367	0.2937	0.3747	0.2896	0.3698	0.2961

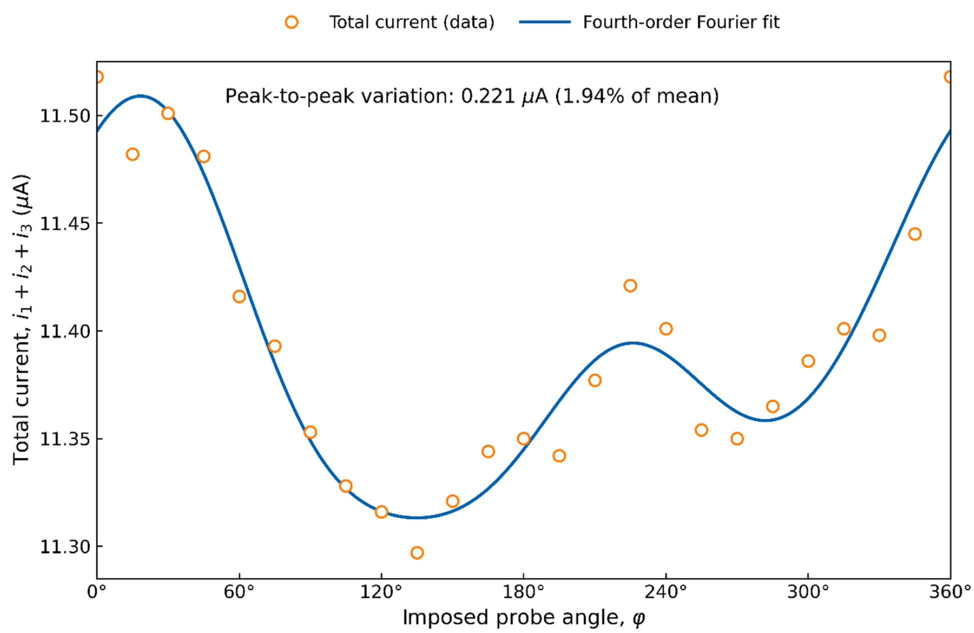

Fig. 13. Total current variation with probe orientation (A3): evidence of geometric/assembly non-idealities.

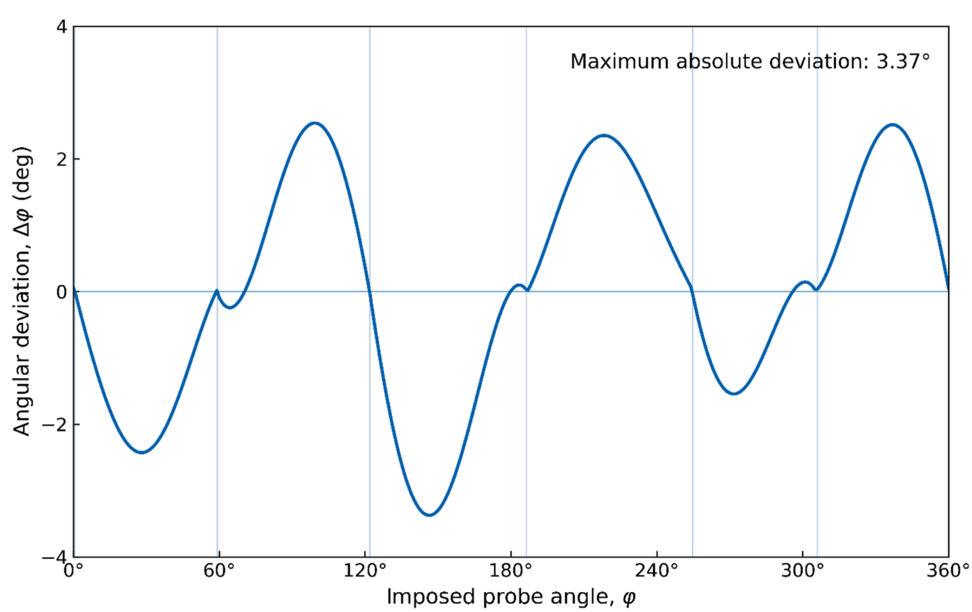

Fig. 14. Angular deviation of the linearized reconstruction from the imposed probe angle for the real three-sector probe. The vertical lines indicate the section boundaries used by FastAngle3.

Table 5
Sensitivity of the reconstructed flow angle to imposed sector-current deviations at the bounding points of ideal three- and four-sector probes.

	I_1	ε, %	ΔI_1x1000	$\Delta\varphi$, deg
3-sector probe	0.384	3	7.1	3.9
	0.384	6	14.2	7.8
	0.276	3	6.0	3.3
	0.276	6	12.0	6.6
4-sector probe	0.315	3	6.5	4.1
	0.315	6	12.9	8.1
	0.243	3	5.5	3.5
	0.243	6	11.0	6.9

4. Discussion

This paper presents a comprehensive analytical framework for circular-sector electrodiffusion probes applicable in practice. Directional calibration and application of directional characteristics of these probes are presented for steady or quasi-steady flow conditions. In this case, the wall shear rate and its components are unique functions of the measured sector currents. In unsteady flows, the more complex mass transfer problem must be solved. Nevertheless, the boundary-layer approach can still be used as a first-order estimate for more sophisticated methods, such as the inverse problem [31,32] or numerical approaches [29].

It is found that circular sector-type probes can be used for a compact method of "pre-compute once, invert fast". The universal directional coefficients are represented accurately by a low-order Fourier series, enabling online flow-direction reconstruction. The Couette-flow calibration data in Appendix A3 show that, for a real three-sector probe (despite some geometric imperfections), the total currents remain nearly independent of direction (the peak-to-peak variation is about 1.94% of the average value) and that angular reconstruction by the linearized method is accurate to within several degrees.

Among the configurations considered, the three-sector probe offers the most favorable practical compromise. It resolves the complete 0–360° flow direction, has greater directional sensitivity, and exhibits slightly lower noise-to-angle amplification than the four-sector probe. Two-sector probes remain suitable mainly for non-reversing flows because their current ordering does not uniquely identify the direction over the full angular range. Four-sector probes may nevertheless be advantageous when larger, geometrically precise electrodes are required for studying concentration-boundary-layer dynamics and frequency response.

There are three challenges concerning the effects on directional characteristics of sector probes: (a) isolating insertions (gaps) between sectors, (b) radial (perpendicular and longitudinal) components of diffusion, and (c) inertia of the concentration boundary layer. Regarding (a), the finite gaps between sectors attenuate the amplitude of the directional characteristics compared to the ideal case, as demonstrated by the comparison between measured and theoretical DC in Fig. 12. Wein and Wichterle (1989) [28] analysed this effect theoretically. The recent work by Harrandt et al. (2024) [21] on semicircular probes also discusses the influence of the insulation gap position on diagnostic performance, confirming that different probe geometries can refine the sensitivity and accuracy of the measurement. Regarding (b), the radial diffusion effect was evaluated by Geshev and Safarova (1999) [29] and shown to attenuate the DC amplitudes at low Peclet numbers. The correction for radial diffusion, applied in Section 3, reduces the discrepancy between theoretical and measured DC but does not fully account for the remaining differences, which are attributed to the gap effect. Regarding (c), the inertia of the concentration boundary layer limits the frequency response of electrodiffusion probes in unsteady flows. Lamarche-Gagnon et al. (2018) [24] addressed this issue using an inverse-problem approach applied to three-segment probes, demonstrating that both the fluctuating magnitude and direction of the wall shear rate can be accurately recovered, even under strong inertial effects.

The present framework is quasi-steady and is not intended for rapidly unsteady or strongly reversing flows. It is applicable when the characteristic time scale of the wall-shear-rate variation is sufficiently longer than the response time of the concentration boundary layer. Under the archival calibration conditions considered here, the characteristic settling time estimated from a voltage-step response is approximately 1.08 s. This value should be regarded only as an order-of-magnitude indication for the present probe and electrolyte, rather than as a universal threshold. When the flow varies on a comparable or shorter time scale, amplitude attenuation and phase lag become important, and transient inverse modelling or a full convection–diffusion formulation should be used.

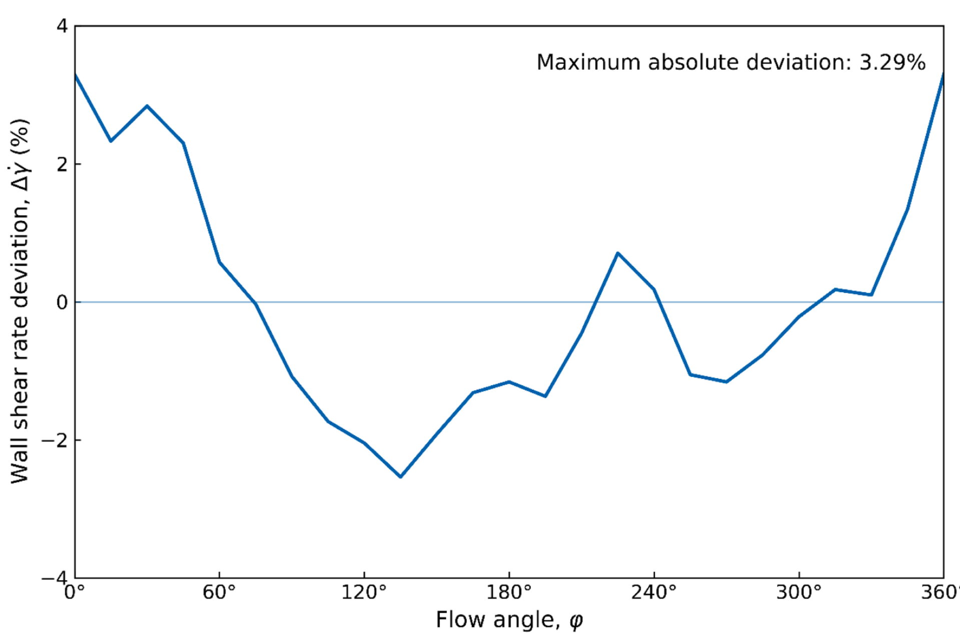

Fig. 15. Wall shear rate deviation as a function of flow angle for real probe.

5. Conclusion

A simple and efficient analytical method for calculating the directional characteristics of circular-sector electrodiffusion probes has been developed within the boundary layer (Leveque) approximation for quasi-steady flows. The method is based on a set of universal coefficients that allow the computation of normalised sector currents for probes with an arbitrary number of sectors and arbitrary sector angles. The key findings are as follows.

(i) The normalised current through a sector of arbitrary size and orientation is expressed by a function G with a single argument, which is computed once and stored as universal coefficients.
(ii) Directional characteristics of ideal two-, three-, and four-sector probes have been calculated and compared. The three-sector probe provides the best combination of angular resolution (slope of 0.104 rad^{-1}) and robustness to current noise.
(iii) A fast linear algorithm (FastAngle) for online estimation of the flow angle from measured sector currents has been presented and validated, achieving an accuracy better than 1.5° for the three-sector probe and 1.3° for the four-sector probe.
(iv) Validation using archival Couette-flow calibration data for a real three-sector probe at $Pe=5 \times 10^3$ gives a maximum angular deviation below 3.5°. The measured total current shows a peak-to-peak variation of 0.221 μA, corresponding to approximately 1.94% of its mean value. The sensitivity analysis shows that imposed sector-current deviations of 3% produce angular deviations below 3.9° and 4.1° for the ideal three- and four-sector probes, respectively; the corresponding deviations increase for the 6% perturbation cases.

The proposed framework is intended for quasi-steady, high-Péclet-number conditions in which the boundary-layer approximation remains valid, and it provides a practical basis for online data reduction from circular-sector probes used for wall-shear-rate measurement.

CRediT authorship contribution statement

Mouhamad El Hassan: Conceptualization, Formal analysis, Methodology, Validation, Writing – original draft, Writing – review & editing. **Jaromir Havlica:** Data curation, Formal analysis, Writing – original draft. **Walid Blel:** Formal analysis, Methodology, Writing – original draft. **Nikolay Bukharin:** Data curation, Formal analysis, Writing – original draft. **Vaclav Sobolik:** Conceptualization, Data curation, Formal analysis, Methodology, Writing – original draft.

Declaration of competing interest

The authors declare that they have no known competing financial interests or personal relationships that could have appeared to influence the work reported in this paper.

Acknowledgments

The authors received no specific funding for this work.

Appendix

A1) Scilab algorithm for four-sector probes

```
function [ang,k]=FastAngle4(I1,I2,I3,I4)
  if I1≤I2 then if I1>I3 then k = 7; I=I1;
        elseif I4<I1 then k = 6; I=I3;
        elseif I4<I2 then k = 5; I=I2;
          else k = 4; I=I4; end;
    elseif I2>I4 then k = 8; I=I2;
        elseif I3>I1 then k = 3; I=I3;
        elseif I4>I1 then k = 2; I=I1;
          else k = 1; I=I4; end;
  ang=flim(k)+(I-Ilim(k))*(flim(k + 1)-flim(k))/(Ilim(k + 1)-Ilim(k));
flim=[φl1 φu1 φu2 φu3 φu4 φu5 φu6 φu7 φu8];
Ilim=[Il1 Iu1 Iu2 Iu3 Iu4 Iu5 Iu6 Iu7 Iu8];
end; // FastAngle4
```

A2) Scilab algorithm for three-sector probes

```
function [ang,k]=FastAngle3(I1,I2,I3)

  if I1≤I2 then if I2<I3 then k = 3; I=I2;
        elseif I1<I3 then k = 4; I=I3;
          else k = 5; I=I1; end;
    elseif I3<I2 then k = 6; I=I2;
        elseif I3<I1 then k = 1; I=I3;
          else k = 2; I=I1; end;
  ang=flim(k)+(I-Ilim(k))*(flim(k + 1)-flim(k))/(Ilim(k + 1)-Ilim(k));
flim=[φl1 φu1 φu2 φu3 φu4 φu5 φu6];
Ilim=[Il1 Iu1 Iu2 Iu3 Iu4 Iu5 Iu6];
end; // FastAngle3
```

A3) Measured currents $\boldsymbol{i}_j^+$ in μA, total current $\sum \boldsymbol{i}_j^+$ and normalized currents $\boldsymbol{I}_j^+ = \boldsymbol{i}_j^+ / \sum \boldsymbol{i}_j^+$

angle °	i_1^+	i_2^+	i_3^+	$\sum i_j^+$	I_1^+	I_2^+	I_3^+
0	3.072	4.231	4.215	11.518	0.267	0.367	0.366
15	3.071	4.02	4.391	11.482	0.267	0.350	0.382
30	3.106	3.829	4.566	11.501	0.270	0.333	0.397
45	3.205	3.607	4.669	11.481	0.279	0.314	0.407
60	3.366	3.346	4.704	11.416	0.295	0.293	0.412
75	3.594	3.124	4.675	11.393	0.315	0.274	0.410
90	3.814	2.956	4.583	11.353	0.336	0.260	0.404
105	4.029	2.868	4.431	11.328	0.356	0.253	0.391
120	4.212	2.858	4.246	11.316	0.372	0.253	0.375
135	4.385	2.842	4.07	11.297	0.388	0.252	0.360
150	4.557	2.888	3.876	11.321	0.403	0.255	0.342
165	4.689	3.02	3.635	11.344	0.413	0.266	0.320
180	4.758	3.206	3.386	11.35	0.419	0.282	0.298
195	4.758	3.42	3.164	11.342	0.420	0.302	0.279
210	4.7	3.634	3.043	11.377	0.413	0.319	0.267
225	4.572	3.854	2.995	11.421	0.400	0.337	0.262
240	4.393	4.028	2.98	11.401	0.385	0.353	0.261
255	4.192	4.205	2.957	11.354	0.369	0.370	0.260
270	3.971	4.398	2.981	11.35	0.350	0.387	0.263
285	3.728	4.543	3.094	11.365	0.328	0.400	0.272
300	3.467	4.624	3.295	11.386	0.304	0.406	0.289
315	3.253	4.624	3.524	11.401	0.285	0.406	0.309
330	3.105	4.532	3.761	11.398	0.272	0.398	0.330
345	3.051	4.389	4.005	11.445	0.267	0.383	0.350
360	3.072	4.231	4.215	11.518	0.267	0.367	0.366

Data availability

Data will be made available on request.

References

[1] W.E. Ranz, Electrolytic methods for measuring water velocities, AIChE J. 4 (1958) 338–342, https://doi.org/10.1002/aic.690040321.

[2] T.J. Hanratty, J.A. Campbell, Measurement of wall shear stress, in: R.J. Goldstein (Ed.), Fluid Mechanics Measurements, Hemisphere Publishing Corporation, Washington, DC, 1983.

[3] L. Böhm, S. Jankhah, J. Tihon, P.R. Bérubé, M. Kraume, Application of the electrodiffusion method to measure wall shear stress: integrating theory and practice, Chem. Eng. Technol. 37 (2014) 938–950, https://doi.org/10.1002/ceat.201400026.

[4] M. Kristiawan, K. Sodjavi, B. Montagné, A. Meslem, V. Sobolik, Mass transfer and shear rate on a wall normal to an impinging circular jet, Chem. Eng. Sci. 132 (2015) 32–45, https://doi.org/10.1016/j.ces.2015.03.070.

[5] M. Kristiawan, M. El Hassan, A.E. Faye, V. Sobolík, Experimental investigation of Taylor-Couette-Poiseuille flow at low Taylor and Reynolds numbers, PLoS. One 14 (2019) e0212728, https://doi.org/10.1371/journal.pone.0212728.

[6] M. El Hassan, V. Sobolik, A. Chamkha, M. Kristiawan, Kinematics of helical flow between concentric cylinders with axial through flow, Int. J. Heat. Mass Transf. 182 (2022) 121938, https://doi.org/10.1016/j.ijheatmasstransfer.2021.121938.

[7] N. Merabet, A. Mahamdia, Z. Haddad, Taylor-Couette flow dynamics and transitions with immiscible continuous fluids: an electrodiffusion study, Int. Commun. Heat Mass Transf. 166 (2025) 109130, https://doi.org/10.1016/j.icheatmasstransfer.2025.109130.

[8] O.N. Kashinskii, M.A. Vorobyev, Wall shear stress in a model of 3 · 3 rod bundle, J. Engin. Thermophys. 29 (2020) 388–392, https://doi.org/10.1134/S1810232820030029.

[9] M.A. Vorobyev, O.N. Kashinsky, Local characteristics of bubbly flow in rods assembly 3 × 3, Int. J. Heat. Mass Transf. 231 (2024) 125844, https://doi.org/10.1016/j.ijheatmasstransfer.2024.125844.

[10] O.N. Kashinsky, A.S. Kurdyumov, Wall shear stress distribution in an annular channel with a stationary gas bubble, J. Engin. Thermophys. 30 (2021) 646–653, https://doi.org/10.1134/S181023282104007X.

[11] A.E. Gorelikova, O.N. Kashinskii, A.S. Kurdyumov, Effect of the inclination angle on local characteristics of an upward gas-liquid flow in a circular tube, J. Appl. Mech. Tech. Phy. 66 (2025) 728–734, https://doi.org/10.1134/S0021894425700282.

[12] K. Ezeji, J. Tihon, Near-wall flow response to large air bubbles rising in inclined water channels, Chem. Eng. Sci. 247 (2022) 116914, https://doi.org/10.1016/j.ces.2021.116914.

[13] F. Bode, A. Meslem, C. Patrascu, I. Nastase, Flow and wall shear rate analysis for a cruciform jet impacting on a plate at short distance, PCFD 20 (2020) 169, https://doi.org/10.1504/PCFD.2020.107276.

[14] Y. Wang, Y. Tsuji, Characteristics of shear stress fluctuations in polymer solutions and their relation to turbulent structures in channel flows, Phys. Fluids 36 (2024) 105153, https://doi.org/10.1063/5.0230123.

[15] B. Py, Étude tridimensionnelle de la sous-couche visqueuse dans une veine rectangulaire par des mesures de transfert de matière en paroi, Int. J. Heat. Mass Transf. 16 (1973) 129–144, https://doi.org/10.1016/0017-9310(73)90257-3.

[16] C. Deslouis, B. Tribollet, J. Tihon, Near-wall turbulence in drag reducing flows investigated by the photolithography-electrochemical probes, J. Nonnewt. Fluid. Mech. 123 (2004) 141–150, https://doi.org/10.1016/j.jnnfm.2004.07.016.

[17] V. Sobolík, Electrochemical study of Taylor-couette flow by limiting diffusion current method, Collect. Czech. Chem. Commun. 64 (1999) 1193–1210, https://doi.org/10.1135/cccc19991193.

[18] J. Tihon, V. Tovchigrechko, V. Sobolík, O. Wein, Electrodiffusion detection of the near-wall flow reversal in liquid films at the regime of solitary waves, J. Appl. Electrochem. 33 (2003) 577–587, https://doi.org/10.1023/A:1024988602276.

[19] J. Havlica, D. Kramolis, F. Huchet, A revisit of the electro-diffusional theory for the wall shear stress measurement, Int. J. Heat. Mass Transf. 165 (2021) 120610, https://doi.org/10.1016/j.ijheatmasstransfer.2020.120610.

[20] V. Harrandt, D. Kramolis, F. Huchet, J. Tihon, J. Havlica, The electrodiffusional theory for the wall shear stress measurement by two-strip probe, Int. J. Heat. Mass Transf. 212 (2023) 124287, https://doi.org/10.1016/j.ijheatmasstransfer.2023.124287.

[21] V. Harrandt, Y. Bazaikin, F. Huchet, J. Tihon, J. Havlica, Theory for electrodiffusional wall shear stress measurement by directionally sensitive twin semicircular probe, Int. J. Heat. Mass Transf. 235 (2024) 126191, https://doi.org/10.1016/j.ijheatmasstransfer.2024.126191.

[22] C. Deslouis, F. Huet, O. Gil, B. Tribollet, Spectral analysis of wall turbulence with a bicircular electrochemical probe, Exp. Fluids. 16 (1993) 97–104, https://doi.org/10.1007/BF00944911.

[23] V. Sobolík, O. Wein, O. Gil, B. Tribollet, Three-segment electrodiffusion probes for measuring velocity fields close to a wall, Exp. Fluids. 9 (1990) 43–48, https://doi.org/10.1007/BF00575334.

[24] M.-É. Lamarche-Gagnon, V. Sobolík, J. Vétel, Diagnostics of the fluctuating wall shear rate components using an uncalibrated three-segment electrodiffusion sensor, Exp. Fluids. 59 (2018) 168, https://doi.org/10.1007/s00348-018-2623-z.

[25] O. Wein, V. Sobolík, Theory of direction sensitive probes for electrodiffusion measurement of wall velocity gradients, Collect. Czech. Chem. Commun. 52 (1987) 2169–2180, https://doi.org/10.1135/cccc19872169.

[26] O. Wein, V. Sobolík, Segmented electrodiffusion probes: simultaneous measurement of shear rate and normal flow component, Collect. Czech. Chem. Commun. 54 (1989) 3043–3060, https://doi.org/10.1135/cccc19893043.

[27] V. Sobolik, O. Wein, The Levich problem with an eccentric segmented electrode on rotating disk, Russ. J. Electrochem. 44 (2008) 424–433, https://doi.org/10.1134/S1023193508040083.

[28] O. Wein, K. Wichterle, Theory of segmented electrodiffusion probes: the effect of insulating insertions, Collect. Czech. Chem. Commun. 54 (1989) 3198–3212, https://doi.org/10.1135/cccc19893198.
[29] P.I. Geshev, N.S. Safarova, Angular and transient characteristics of circular electrochemical friction probes, Int. J. Heat. Mass Transf. 42 (1999) 3183–3188, https://doi.org/10.1016/S0017-9310(98)00369-X.
[30] A. Lévêque, Les lois de la transmission de chaleur par convection, Ann. Mines Mém. 13 (1928).
[31] F. Rehimi, F. Aloui, S. Ben Nasrallah, L. Doubliez, J. Legrand, Inverse method for electrodiffusional diagnostics of flows, Int. J. Heat. Mass Transf. 49 (2006) 1242–1254, https://doi.org/10.1016/j.ijheatmasstransfer.2005.10.008.
[32] M.-É. Lamarche-Gagnon, J. Vétel, An inverse problem to assess the two-component unsteady wall shear rate, Int. J. Therm. Sci. 130 (2018) 278–288, https://doi.org/10.1016/j.ijthermalsci.2018.04.022.